Ultrathin TiO$_2$(B) Nanorods with Superior Lithium-Ion Storage Performance

Roberto Giannuzzi,[†] Michele Manca,*,[†] Luisa De Marco,[†] Maria R. Belviso,[‡] Alessandro Cannavale,[†] Teresa Sibillano,[§] Cinzia Giannini,[§] P. Davide Cozzoli,[‡,||] and Giuseppe Gigli[†,‡,||]

[†]Center for Bio-Molecular Nanotechnology, Fondazione Istituto Italiano di Tecnologia, Via Barsanti, 73010 Arnesano, Lecce, Italy
[‡]National Nanotechnology Laboratory (NNL), CNR Istituto Nanoscienze, c/o Distretto Tecnologico, Via Arnesano 16, 73100 Lecce, Italy
[§]Istituto di Cristallografia (IC) CNR, via Amendola 122/O, 70126 Bari, Italy
[||]Dipartimento di Matematica e Fisica "E. De Giorgi", Universita' del Salento, Via Arnesano, 73100 Lecce, Italy

S *Supporting Information*
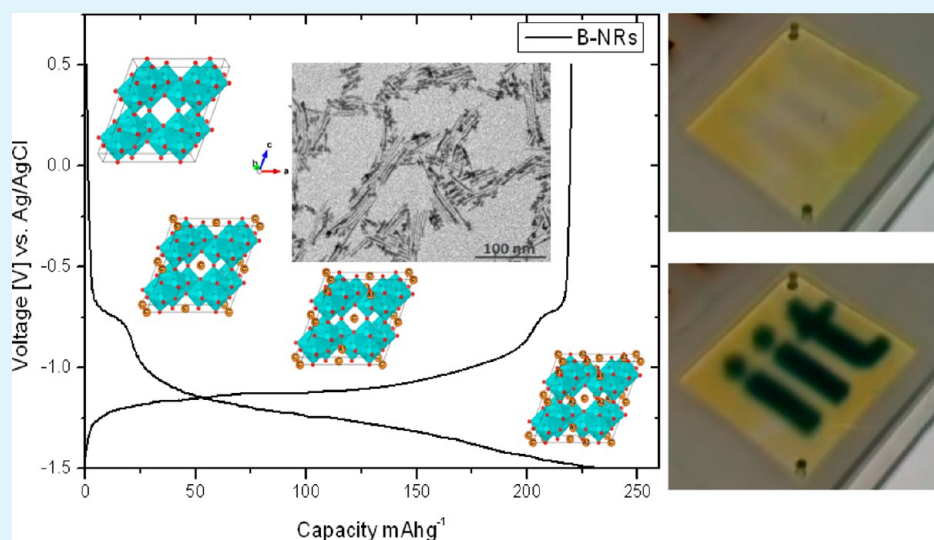
ABSTRACT: The peculiar architecture of a novel class of anisotropic TiO$_2$(B) nanocrystals, which were synthesized by an surfactant-assisted nonaqueous sol−gel route, was profitably exploited to fabricate highly efficient mesoporous electrodes for Li storage. These electrodes are composed of a continuous spongy network of interconnected nanoscale units with a rod-shaped profile that terminates into one or two bulgelike or branch-shaped apexes spanning areas of about 5×10 nm^2. This architecture transcribes into a superior cycling performance (a charge capacitance of 222 mAh g^{-1} was achieved by a carbon-free TiO$_2$(B)-nanorods-based electrode vs 110 mAh g^{-1} exhibited by a comparable TiO$_2$-anatase electrode) and good chemical stability (more than 90% of the initial capacity remains after 100 charging/discharging cycles). Their outstanding lithiation/delithiation capabilities were also exploited to fabricate electrochromic devices that revealed an excellent coloration efficiency (130 cm^2 C^{-1} at 800 nm) upon the application of 1.5 V as well as an extremely fast electrochromic switching (coloration time ∼5 s).

KEYWORDS: *TiO$_2$(B) nanorods, mesostructured electrodes, lithium-ion storage, electrochemical-impedance spectroscopy*

■ INTRODUCTION

Titanium dioxide (TiO$_2$) nanomaterials represent a class of a chemically inert, nontoxic, biocompatible, and inexpensive high-band-gap semiconductors characterized by wide range of interesting chemical-physical properties, including a high refractive index, good electric conductivity, excellent UV-absorption capability, and, in particular, a remarkable (photo)-catalytic activity.[1,2] Because of its particular electronic band structure and photochemical stability, nanoscale TiO$_2$ has been demonstrated to be a suitable platform for many solar-energy conversion applications ranging from dye-sensitized solar cells and water-splitting photoelectrolytic systems for hydrogen production to photocatalysts for the demolition of pollutants and conversion of CO$_2$ into added-valued chemicals and small hydrocarbon fuels.[1] TiO$_2$ has also recently attracted significant attention as an efficient lithium-ion (Li$^+$) anode material

because of its large specific capacity and cycling stability at high charge rates relative to graphite.[3−10]

Among TiO$_2$ polymorphs, monoclinic-phase TiO$_2$(B) is considered to be the most promising candidate for use as an anode material for Li$^+$ batteries (LIBs) because of its fast Li$^+$ loading−extraction properties and high insertion capacity.[7−13] The overall Li$^+$ intercalation/deintercalation mechanism can be described according to the following equilibrium

$$TiO_2 + xLi^+ + xe^- \leftrightarrow Li_xTiO_2 \qquad (1)$$

where x is the insertion coefficient.

The crystal lattice of TiO$_2$(B) is distinguished by a more open framework structure than those of the anatase and rutile counterparts, with accessible channels for Li$^+$ transport perpendicular to the [010] direction, which leads to fast Li$^+$ transport through the lattice. The larger specific capacity relative to other TiO$_2$ polymorphs is due to the lower density of its crystal lattice. The maximum theoretical capacity has been estimated to be 335 mAh g^{-1}, which corresponds to an intercalation coefficient $x = 1$ and to the complete reduction of Ti^{4+} to Ti^{3+} (eq 1). This makes TiO$_2$(B) an alternative anode that is potentially capable of performing competitively with graphite with a theoretical capacity of 372 mAh g^{-1}.[11,12]

Generally, energy-storage devices also require TiO$_2$ to be in contact with a liquid or solid electrolyte. Meso- and nanostructuring is hence a widely adopted strategy to ensure a high contact interface between the Li$^+$-hosting materials and the electrolyte, short diffusion distances for Li$^+$, and easy accommodation of strain during cycling, thus enhancing the capacity, rate performance, and cyclability life. An optimized electrode should be carefully designed to guarantee a high specific surface area, good electron transport, and low charge-carrier recombination losses simultaneously.

The electrochemical performances of TiO$_2$(B) highly depends on the size, shape, crystallographic structure, and architectural arrangement of the crystallites constituting the TiO$_2$(B) materials concerned, which influence the kinetics and reversible capacity for lithiation. In particular, one-dimensional (1D) nanostructures demonstrate excellent Li$^+$ insertion−extraction when compared to nanoparticles and bulk TiO$_2$(B). Therefore, the control over their morphological features and crystallographic orientation is extremely important to ensure fast charging/discharging rates and high capacitance.[13,14]

Armstrong et al.[15] first published a report on the Li$^+$-storage capabilities of TiO$_2$(B) nanowires (which had a diameter ranging from 20 to 40 nm and a length of 2−10 mm) that delivered a capacity as high as 275 mAh g^{-1} at a current density of 10 mA g^{-1}, corresponding to a lithiated phase identifiable as Li$_{0.82}$TiO$_2$. They claimed an improved cyclic stability compared with anatase TiO$_2$. They also reported the effective implementation of TiO$_2$(B) nanotubes with even better charge-accumulation rates by demonstrating a Li$_{0.98}$TiO$_2$ stoichiometry.

More recently, Aravindan et al.[16,17] delivered a good discharge capacity (around 195 mAh g^{-1} at a current density of 150 mAh) and an outstanding cycling profile (up to 500 cycles with a coulumbic efficiency of over 99.5%) through the implementation a batch of TiO$_2$(B) nanorods with a relatively high aspect ratio (~100 nm in diameter and a few micrometers in length).

The top-most rate performance that has been recorded thus far was by Liu et al.[11,18] through the implementation of a hierarchical mesoporous electrode made by TiO$_2$(B) micro-

spheres, which exhibited a double-scale roughness and provided a capacity as high as 150 mAh g^{-1} even after 5000 cycles at a 3350 mA g^{-1}.

Taken together, these results suggest that mesoporous architectures composed of ultrathin low-dimensional TiO$_2$(B) building blocks can provide superior lithiation capabilities because the host material would offer an extremely high surface-to-volume ratio and short pathways to Li$^+$ intercalation/deintercalation across the thickness of the nanocrystalline units.[19]

In addition to Li batteries, the above-mentioned cation insertion/deinsertion mechanism underlies the operation of another popular class of energy-saving devices, namely, electrochromic (EC) windows. These are commonly employed in energy-efficient buildings, rear-view mirrors, sunroofs, and displays because of their ability to change their optical characteristics (darken/lighten) in response to the application of a small electric-potential difference.[20] Their performances still depend on the reversible electrochemical double injection of small cations (such as Li$^+$) and electrons into the host lattice of multivalent transition-metal-oxide materials.[21] Among inorganic materials, tungsten oxides (WO$_x$) have been the most extensively studied. In fact, amorphous WO$_3$ films are capable of providing a high coloration efficiency in the visible region of the electromagnetic spectrum. However, because of their fast dissolution rate in acidic electrolyte solutions, the extended durability of EC films under severe working conditions is still an open issue. Besides this, the relatively low capacitance and the poor rate capability remain as yet insurmountable drawbacks of WO$_3$ bulk when used as an anode material in LIBs and EC windows. Such limitations generally correlate with a corresponding poor availability of open channels to allow efficient ionic and electrical conductivity pathways across the WO$_3$ lattice as well as throughout the overall electrode structure.

In this regard, the potential of nanocrystalline porous TiO$_2$ films in electrochromic devices has been recently explored. Long-term cycling stability has been assessed recently by Ding et al. for a TiO$_2$-anatase electrochromic film.[22] TiO$_2$ offers the considerable advantage that Li$^+$ ions can be reversibly inserted into the lattice with only a negligible volume change accompanying the process. On this basis, TiO$_2$(B), which indeed has a lower density than anatase or rutile, can be reasonably considered as the most suitable candidate to replace WO$_3$ in next generation of highly stable, cost-effective EC devices.

To meet technological requirements, it appears clear that the ability to develop controllable electrode architectures in which the structural and morphological features of the constituent building units provide tailored nanotextures with specific functionalities still represents a crucial challenge towards boosting the performance of a large spectrum of energy-conversion/storage devices. Over the past 2 decades, the development of advanced colloidal routes has enabled selective access to many TiO$_2$ polymorphs in forms as diverse as mesoporous nanostructures and thin films, nanocrystals, nanowires, nanosheets, and nanotubes.[1] Control over crystal structure, size, shape, and mesoporous ordering has been pursued as a means of maximizing both the overall capacity and rate capability of defined low-TiO$_2$ architectures in EC and LIB applications. Among others, surfactant-assisted liquid-phase synthetic approaches have been especially distinguished for their versatility in providing precision-tailored TiO$_2$ nanocryst-

als that can be readily processed into mesoporous thin films suitable for disparate energy-conversion and -storage purposes.[23]

Most of the achievements reported in surfactant-assisted synthetic routes so far have been documented for the anatase, brookite, and rutile phases.[1] Actually, wet-chemically prepared $TiO_2(B)$ nanostructures, which to date have been exploited in energy devices, have been exclusively obtained by surfactant-free hydrothermal routes based on acidic treatment of proton-exchanged potassium titanates[13,16,17,24−29] or controlled hydrolysis of molecular titanium precursors.[30−33]

In this article, we report on the exploitation of a novel class of $TiO_2(B)$ nanorods with bulgelike terminations obtained by a surfactant-assisted nonaqueous sol−gel route to fabricate high-quality nanostructured electrodes that are capable of exhibiting excellent storage capacitance and fast electron-transfer kinetics. A full electrochemical characterization was carried out to elucidate the correlation between the Li^+-storage performance and the intimate structure of the electrodes made by the here-disclosed nanocrystals.

■ EXPERIMENTAL SECTION

Synthesis and Characterization of TiO_2 Nanocrystals. Syntheses were carried out in 100 mL three-necked flasks under air-free conditions using a standard Schlenk line setup. Oleate-capped TiO_2 nanocrystals with a controlled crystal structure and anisotropic morphology were prepared by manipulating the nonhydrolytic condensation reaction of titanium tetraisptropoxide (TTIP) with oleic acid at high temperature. Linear-shaped anatase TiO_2 nanorods (A-NRs) were prepared according to a previously reported protocol.[34] Briefly, 60 mmol of TTIP (Aldrich, 97%) was added to 50 g of degassed oleic acid (Aldrich, 90%) at room temperature. Then, the resulting mixture was heated at 270 °C under nitrogen flux at a rate of about 10 °C min^{-1} and then kept at this temperature for 2 h. Bulge-terminated $TiO_2(B)$ nanorods (B-NRs) were prepared by modifying the synthetic technique as follows: 2 mL of a 1 M TTIP solution in 1-octadecene (Aldrich, 90%) was rapidly injected via a disposable syringe into 10 mmol of degassed oleic acid preheated at 290 °C under nitrogen flux. The mixture was then annealed at 290 °C for 2 h. After synthesis, the extraction and purification of the nanocrystals was carried out under ambient atmosphere. The crude reaction mixture was allowed to cool naturally to room temperature. Acetone was added to induce flocculation of the TiO_2 product, which was then separated upon centrifugation and thoroughly washed with acetone to remove reactant residuals. The purified nanocrystals were finally dispersed in toluene, providing stable, optically clear colloidal solutions. The size and morphological features of the as-synthesized nanocrystals were inspected by low-resolution transmission electron microscopy (TEM) with a JEOL JEM 1011 microscope operated at 100 kV. Samples for TEM analysis were prepared by dropping a dilute toluene solution of freshly prepared nanocrystals onto carbon-coated copper grids and then allowing the solvent to evaporate. X-ray diffraction measurements were performed using a Bruker D8 Discover diffractometer equipped with a Göbel mirror using Cu Kα radiation ($\lambda_{K\alpha1}$ = 1.54056 Å and $\lambda_{K\alpha2}$ = 1.54439 Å) and a scintillation detector. The working conditions were 40 kV and 40 mA. Data were collected in the range of 10−100°, with a step size of 0.05°. XRD patterns were analyzed with a whole-profile Rietveld-based fitting program (FULLPROF) using a procedure described elsewhere.[35,36] The phase composition of the samples and mean coherent crystal domain size along the relevant crystallographic directions were determined by fitting the patterns to the crystal structure models of monoclinic $TiO_2(B)$ (ICSD no. 41056: space group C2/m; cell parameters: a = 12.17871 Å, b = 3.74122 Å, c = 6.52495 Å; α = β = 90°, γ = 107.0544°) and tetragonal anatase TiO_2 (ICSD no. 154603: space group I41/amd; cell parameters: a = b = 3.7835430 Å, c = 9.614647 Å; α = β = γ = 90°).[36] The phase purity of the samples could be confirmed with an accuracy of ≤5−7% w/w.

NRs-based mesoporous films were prepared according to a procedure described elsewhere.[36,37] Briefly, nanocrystal suspensions were added to an ethylcellulose (Aldrich, 5−15 mPa·3 s, 5% in toluene/ethanol 80:20 v/v; degree of ethoxylation: 48%) solution in toluene (10% w/w) and stirred at 60 °C for 6 h. Then, solvent exchange was carried out as follows: α-terpineol (Aldrich, 99.5%) was added, and the resulting mixture was stirred again for 1 h. Finally, toluene was removed by a rotary evaporator to obtain pastes suitable for doctor-blade deposition. Pastes were thus deposited onto F-doped tin oxide (FTO) conducting glass by doctor blade and gradually heated in an oven under air atmosphere according to the following temperature gradient: 170 °C for 40 min, 350 °C for 15 min, and, finally, 430 °C for 30 min. The morphology of the films was investigated by scanning electron microscopy (SEM) measurements performed with a FEI NOVA nanoSEM 200 microscope. The thickness of the thin-film electrodes was measured with a Tencor Alpha-Step 500 surface profiler. The effect of the thermal treatment on the crystal structure was examined by acquiring XRD patterns of thin films made of sintered nanocrystals that had been assembled on Si substrates using the same procedure as that used for fabricating FTO-supported photoelectrodes. These measurements were performed on the same diffractometer as described above. The patterns were collected at a fixed incident angle of 3° while moving the detector over the 10−100° range with a step size of 0.05°. The XRD data were analyzed as described above.

Electrolyte Preparation. All chemicals and solvents used were of reagent grade and purchased from Aldrich. In all experiments, the electrolyte solution consisted of 1 M $LiClO_4$ in acetonitrile. The solvent was prepared by statically drying anhydrous acetonitrile (Aldrich; initial water content of <50 ppm) over activated 3 Å molecular sieves (200, 48 h). Anhydrous $LiClO_4$ (Aldrich) with an initial water content of <1% was vacuum-dried (180 °C, 48 h), then mixed with the solvent in a glovebox, and stored in Sure Seal bottles (Aldrich) under argon atmosphere.

Electrochemical Characterization. Electrochemical measurements were performed using a three-electrode system connected to a potentiostat/galvanostat (PGSTAT 302N Autolab, Eco-Chemie, The Netherlands). The vessel and mounted electrodes were dried overnight at 110 °C and purged with dry argon for several hours before the electrolyte was added. The electrolyte (100 mL) was injected into the chamber using Omnifit Teflon tubing with connections for chromatography. The counter electrode consisted of a platinum electrode. The reference electrode was an Ag/AgCl wire in saturated LiCl (Merck) dissolved in anhydrous acetonitrile. The potential of this electrode was −0.05 V versus Ag/AgCl. The LiCl was dried at 200 °C for several weeks before use. All measured potentials were referenced to the Ag/AgCl electrode, as has been already reported elsewhere.[38,39] Each electrode was preheated at 450 °C in air for 10 min and then transferred directly to the electrochemical cell in a desiccators. Impedance spectra were recorded using a 10 mV amplitude ac potential between 1 and 10 mHz with 10 points per decade. Spectra were recorded consecutively at 0 to −1.6 V versus Ag/AgCl with 0.2 V intervals after applying the potential for 1800 s, allowing the films to attain steady state.

Electrochromic Cells. Purposely designed electrochromic devices were fabricated by interfacing an ITO-coated glass (10 Ω sq^{-1} from Xinyan Ltd) onto a nanostructured TiO_2 film (thickness: 4 μm; active area: 1 cm^2) deposited onto an FTO-glass (15 Ω sq^{-1} from Xinyan Ltd). The electrodes were assembled into a sandwich-type cell and sealed with a Surlyn hot-melt 50 mm thick gasket. A liquid electrolyte (1 M LiI in 3-methoxypropionitrile) was introduced into the cell gap through a hole that was predrilled on the back of the ITO-coated glass. The hole was sealed using Surlyn hot-melt film and a cover glass. Optical transmittance spectra of the devices were measured by a Varian 5000 spectrophotometer in a wavelength range between 300 and 2500 nm. Coloration/bleaching responses were obtained upon applying an external voltage to the cells through a Keithley 2420 source meter. Coloration/bleaching times were measured at 633 nm.

■ RESULTS AND DISCUSSION

Synthesis of Phase-Controlled Nanorods and Their Processing into Nanostructured Electrodes. For the purposes of the present study, a modified nonaqueous sol–gel route based on the nonhydrolytic condensation of titanium tetraisopotropoxide (TTIP) and oleic acid[34] was exploited to generate two sets of crystal-phase-controlled TiO_2 nanorods capped with a hydrophobic shell of oleate anion ligands. In colloidal surfactant media, anisotropic development of nanocrystals of tetragonal monoclinic anatase[1,34,36,37,40] and $TiO_2(B)$[13,16,17,24−33] is known to be inherently favored by the low symmetry of the respective crystal habits and by the facet-preferential binding of the selected surfactant molecules under kinetically overdriven growth conditions.[1]

Representative TEM images of the as-prepared nanocrystals and SEM images of thermally sintered thin-film electrodes are shown in Figure 1, panels a,b and c,d, respectively.
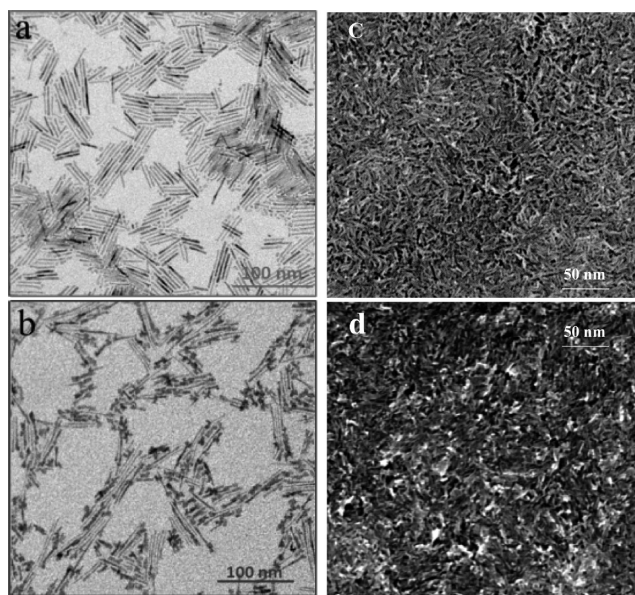
Figure 1. Low-magnification TEM images of the as-synthetized A-NRs (a) and bulge-tipped B-NRs (b). SEM images of sintered films derived from the corresponding A-NRs (c) and B-NRs (d).

Corresponding experimental XRD patterns are reported in Figure 2, panels a and b, respectively. The mean apparent crystal domain sizes along the most relevant crystallographic orientations were estimated by fitting the patterns through a
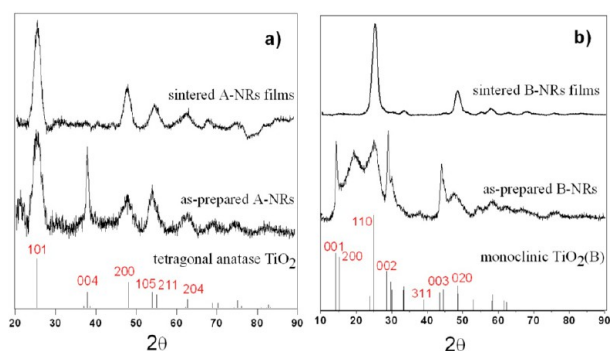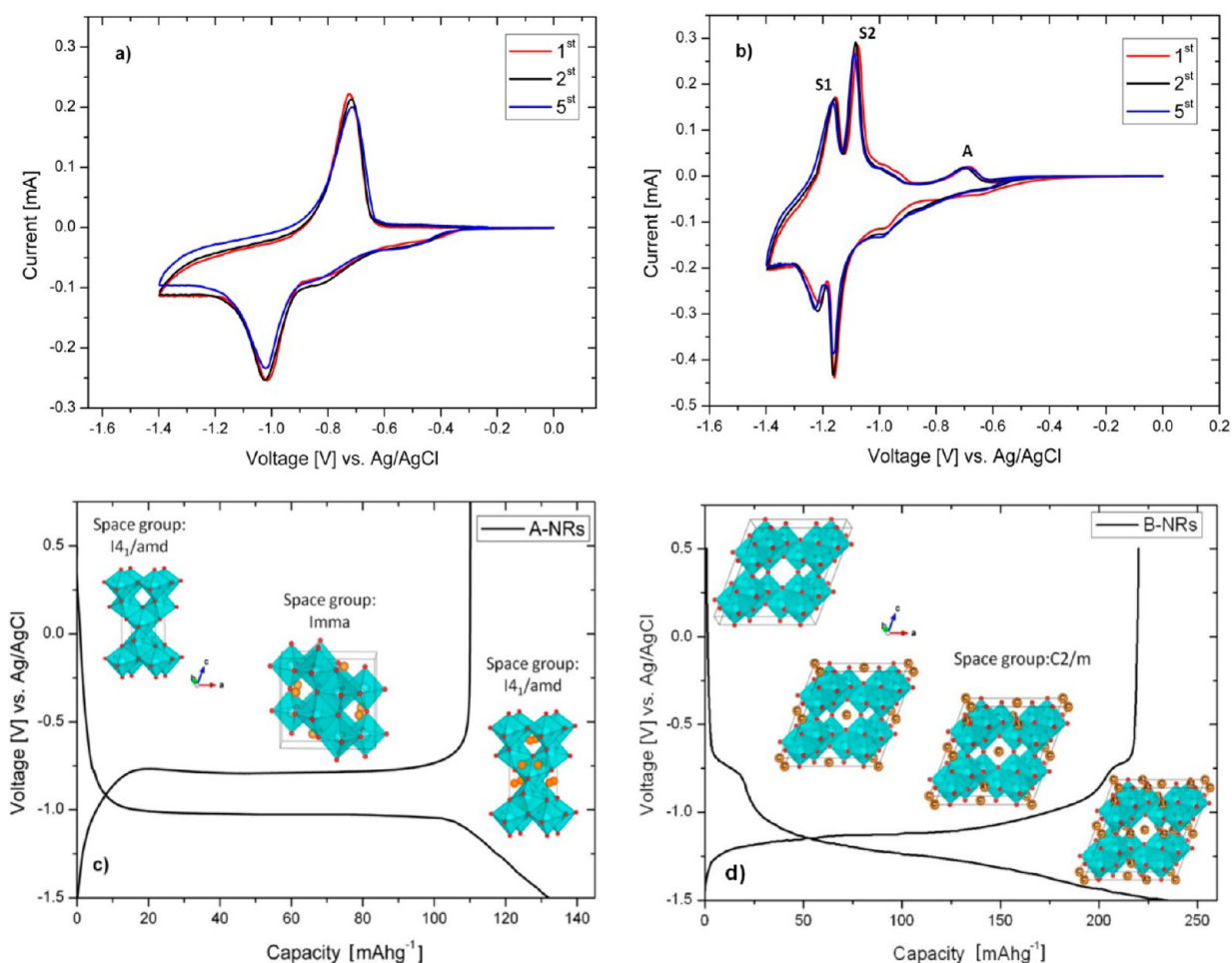
Rietveld-based approach.[35,36] The most meaningful fitting curves and lattice parameters are reported in Figure S1 and Table S1, respectively, in the Supporting Information. One family of nanocrystals is composed of high-aspect-ratio linear-shaped nanorods with an average size of 3×50 nm^2 (Figure 1a) made of the anatase TiO_2 structure (A-NRs). The XRD profile of A-NRs powders (Figure 2a) and quantitative Rietveld-based analysis of the data confirmed the structural identity and the phase purity of the samples. The broad line widths are consistent with the formation of nanosized crystalline domains. The comparatively higher intensity and sharper (004) reflection indicates a preferential crystal elongation in the c-axis direction of the anatase lattice.[1,34,36] This is consistent with the results of quantitative Rietveld-based analysis of the XRD line broadening (Figure S1 and Table S1 in the Supporting Information) that show that the mean coherent crystal domain size is the largest along the [001] direction (12.7 ± 0.5 nm) and is much smaller in the orthogonal [100] (3.7 ± 0.5 nm) direction, in agreement with previous findings.[36] The other family of nanocrystals includes anisotropic nanostructures trapped in the monoclinic $TiO_2(B)$ phase (B-NRs), which are characterized by a more complex topology (Figure 1b). These B-NRs are individually built of a central straight $2−4 \times 40−50$ nm^2 rodlike section, which terminates into one or two bulgelike or branch-shaped apexes spanning areas of about 5×10 nm^2. The relatively uniform TEM contrast featuring the hybrid morphological profile of the B-NRs suggest that their stem and arm sections are not arranged three-dimensionally relative to one another but conform to a planar geometry with uniform thickness. A study on the formation mechanism of these $TiO_2(B)$ nanostructures will be reported elsewhere.[40]

Quantitative crystal-phase composition analysis of the relevant XRD data (Figure 2b) supported the substantial phase purity of the sample. The pattern of the B-NRs powders (Figure 2b), characterized by asymmetric line broadening and prominent (001), (002), and (003) reflections compared to those expected for bulk, suggests a preferential lattice growth in the c-axis direction of the monoclinic $TiO_2(B)$ lattice. The results of Rietveld-based analysis of the XRD pattern[35,36] (Figure S2 and Table S2 in the Supporting Information) reveal that the mean coherent crystal domain size in the B-NRs is the largest along the [001] direction (9.8 ± 0.7 nm) and is the shortest in the [110] (2.3 ± 0.7 nm) and [010] (2.8 ± 0.7 nm) directions, respectively, with [010] being the direction along which channels suitable for Li^+ intercalation are accommodated. When combined with TEM observations, this fact indicates that the B-NRs can actually be regarded as rather flat, anisotropic nano-objects, of which the underlying $TiO_2(B)$ lattice develops the most along the c-axis direction and exhibits a comparatively much smaller extension in the orthogonal [010] direction.

These colloidal nanorods were thus exploited as building blocks to fabricate high-quality mesoporous electrodes serving as Li^+-intercalation hosts. A suitable screen-printable paste was formulated by mixing a toluene solution of the as-synthesized surfactant-capped nanocrystals with ethylcellulose and α-terpineol in appropriate proportions.[36,37] The uniformly dispersed state of the three components allowed ethylcellulose and α-terpineol to serve as effective protective-binding and solvating agents, respectively, for the nanocrystals. The TiO_2-based pastes were deposited on FTO-coated glass and finally subjected to thermal annealing in air to remove the organic components and to induce crystal sintering. The active area of the electrodes was set to 1 cm^2. SEM inspection of the resulting

Figure 2. XRD patters of the as-synthesized nanocrystals and corresponding sintered thin films: (a) A-NRs and (b) B-NRs.

Figure 3. Cyclic voltammogramms recorded at scan rate of 1 mV s^{-1} for the A-NRs (a) and B-NRs electrodes (b). The notations S1, S2, and A in panel b refer to the CV peaks of pseudocapacitive behavior and solid-state diffusion, respectively. First charge-discharge profiles at a current rate of 0.5 C and phase transition upon Li insertion of the TiO$_2$ anatase (c) and TiO$_2$(B) electrode (d) (gray, Ti; red, O; and orange, Li).

sintered films (Figure 1c,d) reveals regular thickness and homogeneous texture over an area of several square micrometers. The films are composed of a continuous spongy network of individually distinguishable, interconnected nanoscale units with a rod-shaped profile resembling that of the original nanorods. Such nanocrystal building blocks are frequently accommodated with their longitudinal axis preferentially lying parallel to the substrate underneath. Notably, although the XRD profiles of the sintered A-NRs and B-NRs films still match with those of the bulk anatase and TiO$_2$(B) references in their respective cases, the original XRD signature of the shape anisotropy appears to have been substantially attenuated. In fact, patterns of the sintered films (Figure 2) demonstrate a reduced number of reflections (note the abatement of the (004) peak of anatase for the A-NR films and of the (001), (002), and (003) peaks of TiO$_2$(B) for the B-NRs films) and noticeable changes in their relative intensities and line widths. Quantitative Rietveld analysis of these XRD data (Figure S1 and Tables S1 in the Supporting Information) reveals the existence of nearly isotropic-shaped crystalline domains with smaller average sizes (in the ranges of 3.3−7.4 and 4.7−6.0 nm for A-NRs and B-NRs films, respectively.) Note that the B-NRs films still featur a small coherent crystal domain size in the [010] direction of about 6.0 ± 0.7 nm,

which should ultimately correlate with their Li$^+$-storage properties.

Taking into consideration that the annealed nanorods incorporated in the films substantially retain their original anisotropic shape profile, as imaged by SEM (Figure 1c,d), the significant modifications in their XRD patterns suggest that relevant microstructural changes have been generated into the TiO$_2$(B) lattice during the thermal-sintering step. These could include the conversion of the original crystal habit into a more polycrystalline-like structure made of smaller isotropic domain subunits (<6.0−7.5 nm, as determined above)[36,41] or an altered degree of crystallinity and lattice strain because of defect annealing and surface restructuring.[36] The effect of the preferential nanorod orientation within the films could further contribute to affect XRD features.[36,41]

Electrochemical Characterization and Rate Performance. The above-described nanostructured films were subjected to a full electrochemical analysis (both under dc and ac conditions) in view of their potential implementation as a Li-battery anode.

Figure 3 displays representative cyclic voltammograms of A-NRs (Figure 3a,c) and B-NRs (Figure 3b,d) films, respectively. In regard to anatase, the first scan shows two well-defined current peaks at about −1 V (along the cathodic sweep) and at −0.7 V (along the anodic sweep), which are in good agreement

with previously reported studies.[42] The cathodic peak at −1 V features the phase transition from tetragonal anatase to orthorhombic $Li_{0.5}TiO_2$, which corresponds to the insertion coefficient x in eq 1 reaching ∼0.5.[43,44] A spontaneous phase separation into lithium-poor $Li_{0.01}TiO_2$ and lithium-rich $Li_{0.5}TiO_2$ occurs at this stage. This process takes place at constant bias voltage, where two phases coexist at the equilibrium and Li^+ ions flow continuously in between them.[43] It can be also observed that no irreversible processes take place in the first cathodic scan, whereas in the successive cycles, the slight reduction in the net area under the curve may indicate a small amount of capacity fading. Then, a shoulder in both the current-potential curves of two nanocrystalline electrodes appears in the range between −0.8 and −1.0 V, which corresponds to the electrons filling the energy states below the conduction-band edge.[45−48] However these trap states do not influence the cycling behavior of the sample.

Cyclic voltammograms for the B-NRs electrode are reported in Figure 3b. The typical pseudocapacitive fingerprint of lithium intercalation in the $TiO_2(B)$ phase is identified by two pairs of peaks located around −1.1 and −1.2 V (denoted as peaks S1 and S2). Nanostructuring $TiO_2(B)$ also enhances the resolution of the double insertion/extraction peaks. The presence of a small amount of contaminating anatase (below the detection limit of our XRD analyses), which may have originated during the sintering process, is revealed by the presence of a weak peak at −0.7 V (denoted as peak A). Thermal sintering at 430 °C may, in fact, be expected to induce the formation of a secondary anatase phase upon transformation of the metastable $TiO_2(B)$.[9,49] However, because the percentage of anatase phase can be expected to be less than 5−7% w/w (i.e., the weight percentage accuracy of our quantitative phase analysis of XRD data), its impact on the electrochemical response of the $TiO_2(B)$ electrode will be henceforth neglected.

When compared to the anatase electrode, $TiO_2(B)$ exhibits a smaller potential separation between the Li^+-insertion and -extraction peaks (ΔE_p = 80 mV for $TiO_2(B)$ and 300 mV for anatase) and a larger overall capacity across a wide potential range. The reduced peak separation can correlate with a more favorable mass transport of the liquid electrolyte throughout the voids of the nanostructured electrode as well as with a more efficient Li^+ diffusion into the nanocrystalline domains.

Figure 3c,d report the profiles of the first charge/discharge cycles of A-NRs- and B-NRs-based electrodes at a current rate of 0.5 C (1 C = 335 mAh g^{-1}).

In the case of A-NRs films, the discharge curves clearly show that the Li^+-insertion process proceeds through three different stages.[50] The first stage, corresponding to the formation of the conductive Li_xTiO_2 in the solid-solution domain, is marked by the sharp decrease in the potential from the open-circuit voltage value to ∼ −1 V, which is reached just before the onset of the plateau region. The second stage, attributable to the well-known two-phase switching mechanism described above, corresponding to the short horizontal plateau region, represents the process of Li^+ insertion into the vacancy sites of the TiO_2 crystal structure. The third stage is the gradual decay of the voltage after the plateau region, reflecting further insertion of lithium ions into the near-surface layer. At the first scan, the A-NRs electrode exhibits a charge capacity of 132 mAh g^{-1} and a subsequent discharge capacity of 110 mAh g^{-1}, which corresponds to a capacity loss of 17%.

On the other side, a major contribution to the charge accumulation in the $TiO_2(B)$ electrode comes from the pseudocapacitive behavior recorded in the range between −0.7 and −1.5 V (Figure 3d). The first insertion cycle at 0.5 C gave a charge capacity as high as 240 mAh g^{-1} and a subsequent discharge capacity of 222 mAh g^{-1}, thus resulting in an irreversible capacity loss of less than 8%. This is an outstanding result if one considers that TiO_2B, like other titanium dioxide polymorphs, has a limited rate capability owing to itse poor electron transport when utilized as a host for Li-ion intercalation. A larger amount of conducting additives is generally required to obtain high rate performance, which, however, reduces the volumetric energy density of the nanostructured TiO_2B electrode materials. Many efforts have been recently made to improve the electronic conductivity of TiO_2-based electrodes by introducing a second conductive phase, such as Au, Ag, and Sn,[51,52] metal oxides like RuO_2,[53] and various carbon-based materials including graphene sheets[7,54] or graphitized carbon.[55−57]

It should be stressed that in these experiments we did not use any additional conductive material: the impressive rate performances achieved by our B-NRs electrodes are solely due to the intelligent morphology tailoring that allowed for the maximization of the electrochemical properties of the film. Cyclic voltammograms of the $TiO_2(B)$ electrode were also measured at different scan rates (Figure 4a). As is commonly observed in many published works when the overall size of $TiO_2(B)$ is shrunk on the nanoscale, both the reduction and oxidation peaks are split into double peaks.
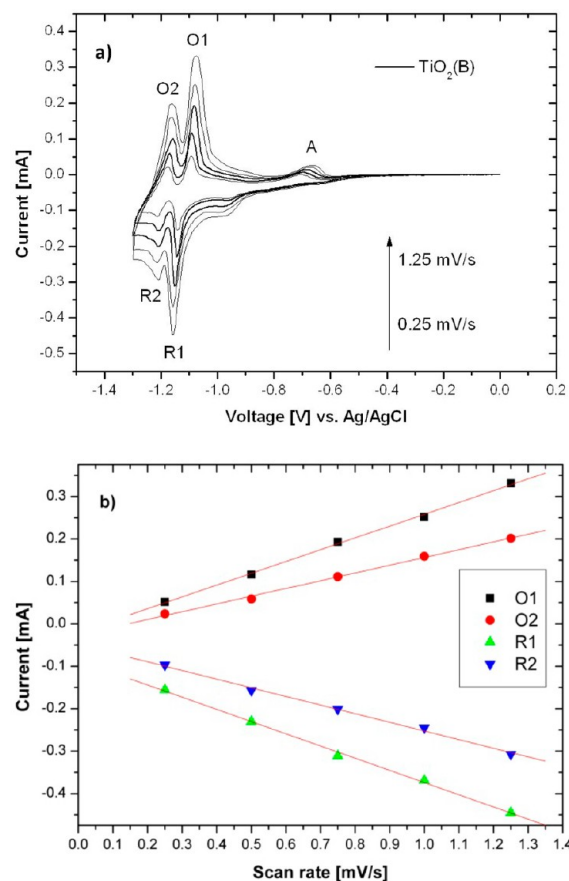
Figure 4. Scan-rate-dependent CVs of the B-NRs electrode (a) and peak current versus scan rate for the labeled oxidation and reduction peaks of the B-NRs electrode (b).

1938

dx.doi.org/10.1021/am4049833 | *ACS Appl. Mater. Interfaces* 2014, 6, 1933−1943

Plots of peak potential versus scan rate are showed in Figure 4b. The general relationship between current and scan rate can be described by the following equations[12,58]

$$i_{CAP} = (dV/dt)C_\phi = \nu C_\phi \qquad (2)$$

$$i_{FAR} = 0.4958nFAc(D\alpha nF\nu/RT)^{1/2} \qquad (3)$$

where C_ϕ is the surface capacitance, ν is the scan rate, n is the number of electrons, F is the Faraday constant, A is the electrode area, c is the concentration, D is the diffusion coefficient, α is the transfer coefficient, R is the gas constant, and T is the temperature. Equation 2 describes the capacitive current resulting from surface processes (pseudocapacitance), which is linearly proportional to the scan rate. Equation 3 describes the current resulting from normal diffusion-controlled Faradaic Li$^+$-insertion processes, which is proportional to the square root of scan rate. An estimation of the surface capacitance contribution is reported in Figure S5.

The electrodes were then subjected to a series of 10 charge/discharge cycles at variable current rates: the rate-performance plot is shown in Figure 5a. The B-NRs electrode exhibits a noticeable capacitance value (222 mAh g^{-1}) at the first discharge run, which is maintained almost invariant even after 10 cycles (212 mAh g^{-1} at the tenth cycle). This means that practically no irreversible capacity loss takes place after the second cycle. In contrast, the A-NRs electrode exhibits a remarkable capacity fading at all rates. At current rates of 0.5, 1,
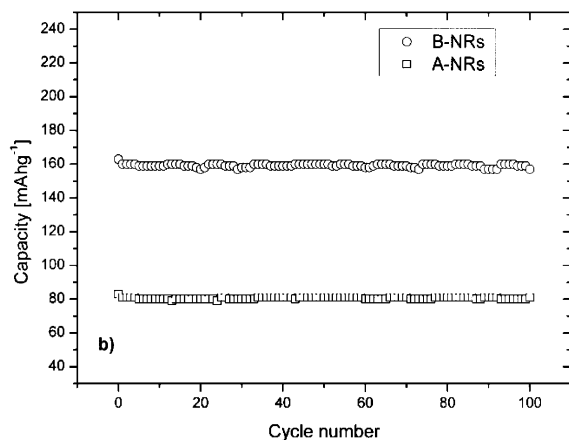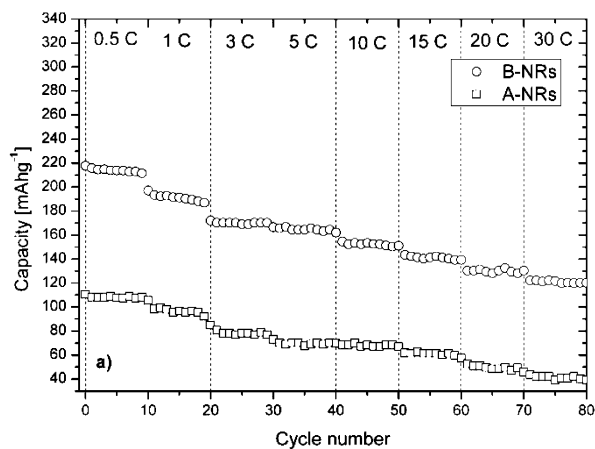
and 5 C, specific capacities of 108, 100, and 80 mAh g^{-1} were detected, respectively.

At high current rates, the difference in capacity between the two polymorphs is further accentuated. The superior cycling performance of TiO$_2$(B) can be attributed to its structural stability as well as to the efficiency with which it can accommodate the strain generated by volume changes during the lithium insertion−extraction processes[24] (Figure S4 in the Supporting Information).

A cyclability test at a charging rate of 10 C was also carried out to evaluate the capacity loss after 100 cycles (Figure 5b). A pre-aging treatment was performed at 0.5 C for five cycles before running 100 charging cycles at 10 C. As can be observed from Figure 5b, both the A-NRs and B-NRs electrodes are capable of preserving more than 90% of their initial capacity.

We then performed a series of electrochemical-impedance spectroscopy (EIS) measurements with the aim of elucidating the impact of the nanocrystalline structure on the charge-transfer kinetics and mass-transport phenomena occurring during the intercalation process. The Nyquist plots of both A-NRs and B-NRs films measured under different bias conditions (from −0.8 to −1.3 V) are reported in Figure 6. Both of them
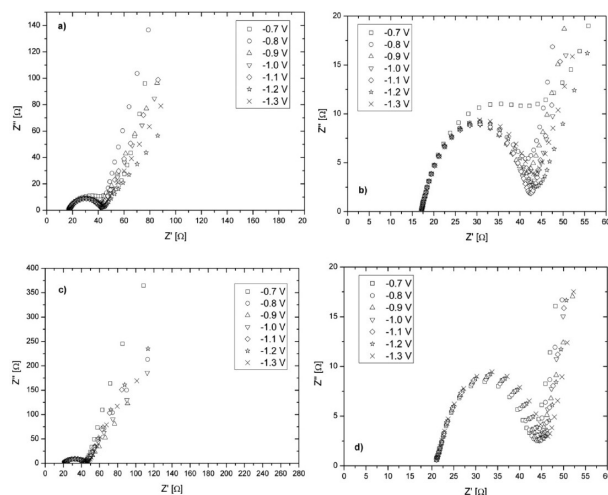
Figure 6. Nyquist plots of B-NRs (a, b) and A-NRs (c, d) nanostructured electrodes at different charge voltages.

conform to the typical EIS spectra of lithium-storing electrodes that do not experience the formation of any passivation layer at the interface with the electrolyte.[50]

Keeping in mind the fundamental electrochemical steps involved in the electrode charging, which generally lie on broadly different time scales and hence are characterized by remarkably different time constants, the experimental Nyquist diagrams can be interpreted in accordance with the following arguments: (i) the pronounced semicircle at high-to-medium frequencies is ascribable to the charge-transfer phenomena, (ii) the straight line at approximately 45° off the real axis in the low-frequency range corresponds to semi-infinite Warburg impedance, and (iii) the steep sloping line at the lower frequencies corresponds to the finite-space diffusion process or the differential intercalation capacity of the electrode. The high-frequency intercept on the real axis corresponds to the ohmic resistance of the cell that is contributed mainly by the electrolyte and the electrode.

Figure 5. (a) Rate performance of the mesoporous B-NRs and A-NRs electrodes at different current rates. (b) Cycling of the charging process at a high current rate of 10 C.

The steps involved in the Li$^+$-intercalation/deintercalation processes, which contribute to the overall response to a small ac perturbation, are (i) the electron injection at the host material/current collector interface, (ii) the diffusion of Li$^+$ ions from the bulk electrolyte the host material, (iii) the charge transfer of Li$^+$ ions through the electrode/electrolyte interface, and (iv) the solid-state transport of Li$^+$ ions in the material matrix, including solid-state diffusion of Li$^+$ ions through the solid phase and occupation of Li$^+$ ions in the lattice.

At this point, the main challenge posed by the interpretation of the impedance data is the identification of a suitable equivalent circuit that should be consistent with the processes occurring in the electrode. Thus far, various electrochemical models have been proposed to analyze the impedance response of an intercalating system.[59−62]

One of the most commonly adopted equivalent circuits is shown in Figure 7a. Here, the solid-state diffusion of Li$^+$ ions
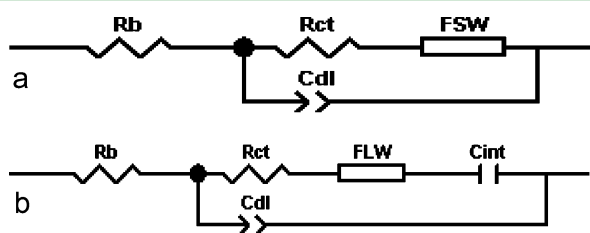
Figure 7. Equivalent circuits adopted in the analysis of electrochemical impedance spectra.

into the thin oxide layer is described through a simple finite-space Warburg element (FSW). Its impedance can be formally expressed through the following equation[63]

$$Z_{FSW} = R_L(j\omega\tau)^{-\alpha} \coth(j\omega\tau)^{\alpha} \tag{4}$$

where R_L is a low-frequency limit of Z' and α is 0.5 for the ideal finite-space behavior.

A careful comparison of the experimental Nyquist plots with the curves fitted by means of the equivalent circuit of Figure 7a reveals the good agreement between them in the high- and low-frequency domains, but no adequately accurate matching was achievable in the medium-frequency region via this model.

Therefore, we considered an alternative distributed finite-space element in place of the FSW and adopted the equivalent circuit, which is shown in Figure 7b. In this case, the medium-frequency domain (which is related to solid-state diffusion in the nanocrystalline TiO$_2$ host) and the low-frequency domain (which is related to the capacitive behavior of the electrode in a quasi-equilibrium regime) are expressed through a serial combination of the finite-length Warburg element (FLW) and the intercalation capacitance, C_{int}.[64,65] The impedance of the FLW can be expressed as

$$Z_{FLW} = R_L(j\omega\tau)^{-\alpha} \tanh(j\omega\tau)^{\alpha} \tag{5}$$

where R_L is the low-frequency limit of Z_{FLW} and α is the ideality coefficient (0.5 for an ideal FLW behavior).

An important difference in the properties of Z_{FSW} and Z_{FLW} should be mentioned: the low-frequency limit of the former quantity is a pure capacitance, whereas the low-frequency limit of the latter quantity is a pure resistance.

To account for the capacitive behavior of a nanostructured electrode, a constant-phase element (Z_{CPE}), which takes into

account a distribution of capacitance values, was used. Z_{CPE} is given by

$$Z_{CPE} = [B(j\omega)^n]^{-1} \tag{6}$$

where B and n ($0 < n < 1$) are frequency-independent proportionality constants.[63] In the limit of $n = 1$, ideal capacitor behavior is observed.

In Figure 8, we plotted the trends of R_{ct} and C_{int} as a function of the bias voltage. Both the A-NRs and B-NRs electrodes
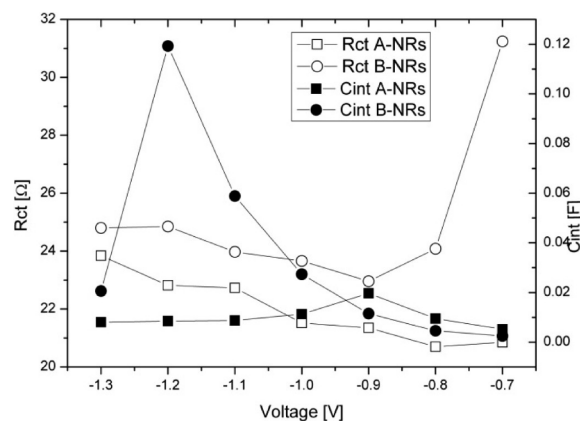
Figure 8. Plot of the charge-transfer resistance and pseudocapacitance of the nanostructured electrodes as a function of the applied voltage.

exhibit a fair amount of charge-transfer resistance on increasing the applied potential (i.e., on increasing the lithium content, x), but no abrupt variations of R_{ct} are observed in the analyzed electrochemical window, meaning that charge-transfer kinetics is not influenced by structural changes in the nanocrystals.

Finally, the diffusive contribution to the mass transport, which is associated with the Warburg impedance element in the equivalent circuit, can be expressed as[66]

$$Z_W = \sigma\omega^{-1/2}(1 - j) \tag{7}$$

where

$$\sigma = V_m(dV_{OC}/dx)/nFA(2D)^{1/2} \tag{8}$$

where ω is the angular frequency, V_m is the molar volume of the electrode material, and σ is the so-called the Warburg prefactor. σ is expressed in Ω s$^{-1/2}$ and is inversely proportional to $D^{1/2}$. Thus, σ can be considered as a resistance barrier for the Li$^+$ diffusion through the solid matrix of the electrode.

From the fitting of the experimental data, it is possible to determine quantitatively the Warburg prefactor, σ, at different bias voltages and hence to extrapolate the diffusion coefficient, D_{Li+}. Figure 9 shows the variation of the Warburg prefactor, σ, as a function of the bias voltage and hence as a function of amount of Li$^+$ intercalated into the crystal. A significant reduction in the Warburg prefactor and hence a remarkable increment of the diffusion coefficient, D_{Li+}, is deduced in the case of the B-NRs electrode.

As expected, Li$^+$ diffusion through TiO$_2$(B) is remarkably faster than through anatase, where it barely propagates across neighboring octahedral sites.[67] This finding is in good agreement not only with theoretical predictions based on the unique lattice structure of TiO$_2$(B)[24,68,69] but also with expectations based on the peculiar architecture of our shape-tailored building blocks. Indeed, in the B-NRs, the channels
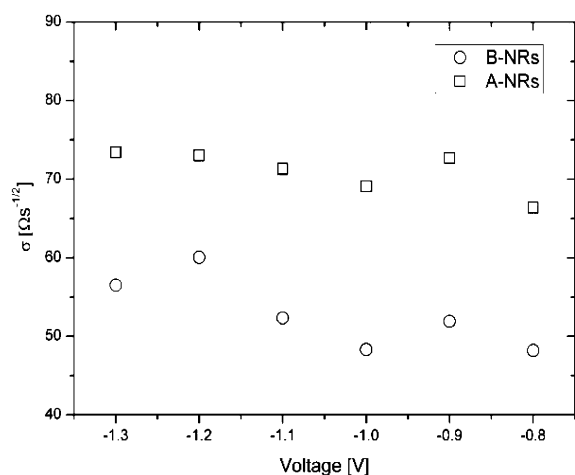
Figure 9. Warburg prefactor as extrapolated from the fitting of the EIS spectra.

along the *b* axis available for Li⁺ intercalation, which lie perpendicular to the longer axis of the nanorod, are rather short (2.8 ± 0.7 nm) and hence offer more favorable conditions for Li⁺ diffusion.

Electrochromic Switching. The above-reported outstanding Li⁺-insertion capability exhibited by the B-NRs was additionally exploited to realize a low-energy-consuming electrochromic device. In this regard, it is useful to recall the fundamental requirements that an electrochromic material should meet to exhibit a fast and effective modulation of optical absorption: (i) The time constant of the ion-intercalation reaction and the length of the diffusion path should be as short as possible to guarantee a prompt response to the electrical input and (ii) the coloration efficiency (CE), which is defined as the change in optical density, ΔOD, per unit of inserted charge, ΔQ, (i.e., $CE = \Delta OD/\Delta Q$), should be as high as possible to provide the largest optical modulation upon insertion or extraction of small charge amounts.

CE is a fundamental figure of merit characterizing electrochromic materials and devices. It can be conveniently expressed by the following equation

$$CE = \frac{\Delta OD}{\Delta Q/A} = \frac{1}{\Delta Q/A} \log\left(\frac{T_b}{T_c}\right) \tag{9}$$

where A is the effective area of the electrochromic electrode and T_b and T_c represent the transmittance in the bleached and colored states, respectively.[70]

TiO$_2$ nanostructured films were deposited onto an FTO-coated glass substrate, sintered at 430 °C, and then adopted as electrochromic electrodes in a sandwich cell filled with 1 M LiI in 3-methoxypropionitrile. The modulation of optical transmittance was measured at different bias voltages in the range between 350 and 1100 nm. The results are shown in Figure 10.

The coloring process is indeed activated at ∼0.5 V. Beyond this value, significant differences in ΔOD are detectable between the two electrodes. As expected, the B-NRs device exhibits a significantly more intense reduction of the transparency with respect to its anatase counterpart. A modulation as high as 70% is achieved in an extremely broad wavelength range (350−1100 nm) upon the application of a bias voltage of only 1.7 V. A complete dark-blue coloration takes place under such conditions. In contrast, a residual transmittance between
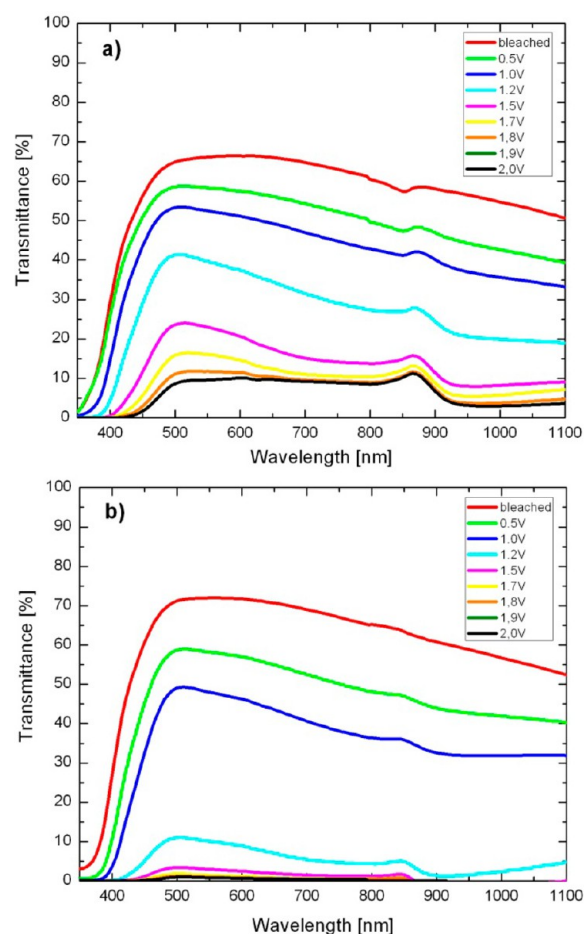
Figure 10. Transmittance spectra of mesoporous A-NRs-based electrodes (a) and B-NRs-based electrodes (b) at different bias voltages.

13 and 23% can be obtained in the case of the A-NRs-based device at the same potential. Demonstrative daylight digital pictures of the B-NRs-based film in the bleached and colored states are shown in Figure 11.
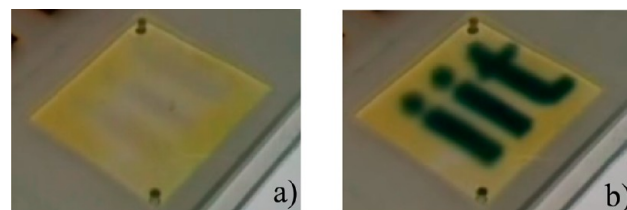
Figure 11. Daylight digital pictures of a B-NRs-based electrochromic device in the bleached (a) and colored (b) states upon the application of 1.7 V.

The switching characteristics of the films were also investigated by in situ monitoring the transmittance at 633 nm. The obtained data are plotted in Figure 12.

The coloration time is less than 5 s for both electrodes, which is much faster than that assessed for the majority of the electrochromic structures so far reported in the literature.[71−73] Such a faster response can be attributed to the large active surface area of the films (Figure S3 in the Supporting Information) as well as to the superior electron-transport properties of the nanostructured TiO$_2$(B) films. In addition, the
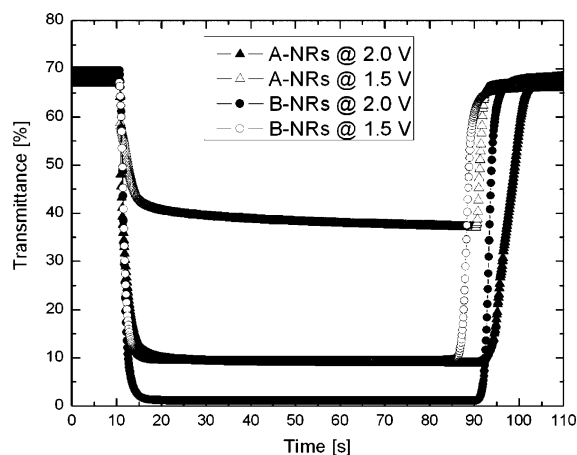
Figure 12. In situ variation of the optical transmittance of the nanostructured A-NRs and B-NRs electrodes measured at 633 nm upon switching the bias voltage on/off.

bleaching process (which occurs upon switching off the applied voltage) is faster in the case of B-NRs, which is evidently correlated to the much stronger dependence of the deintercalation process on the Li⁺-diffusion coefficient of the electrode.

Figure 13 shows the plots of spectral coloration efficiency as a function of the wavelength at two different bias voltages. As is
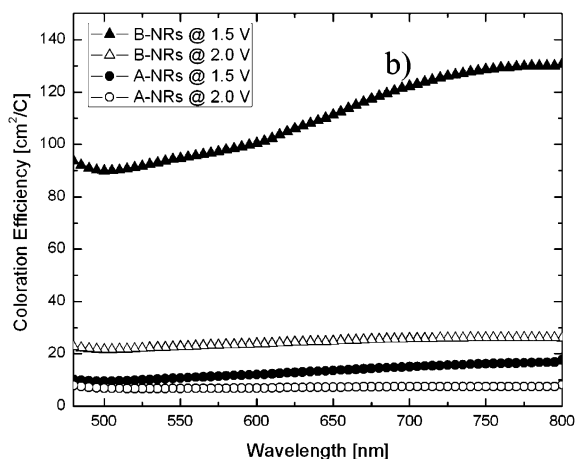
Figure 13. Coloration efficiency of the A-NRs- and B-NRs-based electrodes at two different bias voltages.

known, the CE tends to approach a maximum in the near-infrared region. It is not surprising to find that B-NRs exhibit a superior CE on the basis of the arguments highlighted previously. To the best of our knowledge, the impressive value of CE measured at 1.5 V for the B-NRs, 131 cm^2 C^{-1} at 800 nm, represents the highest value ever recorded for a TiO$_2$-based electrochromic device.

Once again, the superior performance of the B-NRs electrode relative to the A-NRs one deserves to be emphasized. At the same voltage, in fact, the CE of the A-NRs film falls below 20 cm^2 C^{-1} at 800 nm, which is in good accordance with state-of-the-art achievements reported for anatase TiO$_2$.[22]

CONCLUSIONS

We reported the exploitation of a novel class of bulge-tipped TiO$_2$(B) nanorods for the fabrication of mesoporous electrodes acting as efficient Li⁺-storage media. We have compared their performance with that of electrodes fabricated from anatase TiO$_2$ nanorods possessing similar morphological characteristics. The here-disclosed TiO$_2$(B) electrodes offer a noticeable Li⁺-storage capacity, namely, 222 mAh g^{-1} at 0.5 C. It should be stressed that no conductive carbon additives were employed in the fabrication procedure. We demonstrated the effectiveness of this type of nanoarchitecture in achieving an extremely large surface area and a good nanoparticle interconnectivity, which are both responsible for the superior rate capability and faster solid-state Li⁺ diffusion relative to that of the homologous anatase electrodes.

We have also used the TiO$_2$(B) NRs-based films to realize an electrochromic cell. Here, we achieved an excellent coloration efficiency (131 cm^2 C^{-1} at 1.5 V) and an extremely fast optical responsivity. We believe that these results hold great potential for impacting the field of smart electrochromic windows.

ASSOCIATED CONTENT

Supporting Information

Rietveld fits of the XRD data shown in Figure 2; XRD patterns of TiO$_2$−B electrodes before and after electrochemical tests along with additional experimental details of their optical and morphological features. This material is available free of charge via the Internet at http://pubs.acs.org.

AUTHOR INFORMATION

Corresponding Author
*E-mail: michele.manca@iit.it.

Notes
The authors declare no competing financial interest.

ACKNOWLEDGMENTS

REFERENCES

(1) Chen, X.; Mao, S. S. Chem. Rev. 2007, 107, 2891−2959.
(2) Banerjee, A. N. Nanotechnol. Sci. Appl. 2011, 4, 35−65.
(3) Myung, S. T.; Takahashi, N.; Komaba, S.; Yoon, C. S; Sun, Y. K; Amine, K.; Yashiro, H. Adv. Funct. Mater. 2011, 21, 3231−3241.
(4) Huang, S. Y.; Kavan, L.; Exnar, I.; Grätzel, M. J. Electrochem. Soc. 1995, 142, L142−L144.
(5) Pfanzelt, M.; Kubiak, P.; Fleischhammer, M.; Wohlfahrt-Mehrens, M. J. Power Sources 2011, 196, 6815−6821.
(6) Reddy, M. A.; Kishore, M. S.; Pralong, V.; Varadaraju, U. V.; Raveau, B. Electrochem. Solid-State Lett. 2007, 10, A29−A31.
(7) Armstrong, A. R.; Armstrong, G.; Canales, J.; Bruce, P. G. Angew. Chem., Int. Ed. 2004, 43, 2286−2288.
(8) Armstrong, A. R.; Armstrong, G.; Canales, J.; Bruce, P. G. Electrochem. Solid-State Lett. 2006, 9, A139−A143.
(9) Liu, H.; Bi, Z.; Sun, X.G.; Unocic, R. R.; Paranthaman, M. P.; Dai, S.; Brown, G. M. Adv. Mater. 2011, 23, 3450−3454.
(10) Guo, Z.; Dong, X.; Zhou, D.; Du, Y.; Wang, Y.; Xia, Y. RSC Adv. 2013, 3, 3352−3358.
(11) Su, X.; Wu, Q.L.; Zhan, X.; Wu, J.; Wei, S.; Guo, Z. J. Mater. Sci. 2012, 47, 2519−2534.

(12) Dylla, A. G.; Henkelman, G.; Stevenson, K. J. *Acc. Chem. Res.* **2012**, *45*, 1104−1112.

(13) Okumura, T.; Fukutsuka, T.; Yanagihara, A.; Orikasa, Y.; Arai, H.; Ogumi, Z.; Uchimoto, Y. *Chem. Mater.* **2011**, *23*, 3636−3644.

(14) Lee, K. T.; Cho, J. *Nanotoday* **2011**, *6*, 28−41.

(15) Armstrong, A. R.; Armstrong, G.; Canales, J.; García, R.; Bruce, P. G. *Adv. Mat.* **2005**, *17*, 862−865.

(16) Aravindan, V.; Shubha, N.; Cheah, Y. L.; Prasanth, R.; Chuiling, W.; Prabhakar, R. R.; Madhavi, S. *J. Mater. Chem. A* **2013**, *1*, 308−316.

(17) Aravindan, V.; Shubha, N.; Ling, W. C.; Madhav, S. *J. Mater. Chem. A* **2013**, *1*, 6145−6151.

(18) Liu, S.; Jia, H.; Han, L.; Wang, J.; Gao, P.; Xu, D.; Yang, J.; Che, S. *Adv. Mater.* **2012**, *24*, 3201−3204.

(19) Liu, J.; Liu, X. W. *Adv. Mater.* **2012**, *24*, 4097−4111.

(20) Lampert, C. M. *Sol. Energy Mater. Sol. Cells* **2003**, *76*, 489−499.

(21) Granqvist, C. G. *Handbook of Inorganic Electrochromic Materials*; Elsevier: Amsterdam, The Netherlands, 1995.

(22) Dinh, N. N.; Quyen, N. M.; Chung, D. N.; Zikova, M.; VanTruong, V. *Sol. Energy Mater. Sol. Cells* **2011**, *95*, 618−623.

(23) De Marco, L.; Manca, M.; Giannuzzi, R.; Belviso, M. R.; Cozzoli, P. D.; Gigli, G. *Energy Environ. Sci.* **2013**, *6*, 1791−1795.

(24) Armstrong, A. R.; Arrouvel, C.; Gentili, V.; Parker, S. C.; Islam, M. S.; Bruce, P. G. *Chem. Mater.* **2010**, *22*, 6426−6432.

(25) Armstrong, G.; Armstrong, A. R.; Canales, J.; Bruce, P. G. *Chem. Commun.* **2005**, *19*, 2454−2456.

(26) Beuvier, T.; Richard-Plouet, M.; Mancini-Le Granvalet, M.; Brousse, T.; Crosnier, O.; Brohan, L. *Inorg. Chem.* **2010**, *49*, 8457−8464.

(27) Nune, S. K.; Thallapally, P. K.; Dohnalkova, A.; Wang, C.; Liuc, J.; Exarhosc, G. J. *Chem.Commun.* **2010**, *46*, 6801−6803.

(28) Li, J.; Wan, W.; Zhou, H.; Li, J.; Xu, D. *Chem. Commun.* **2011**, *47*, 3439−3441.

(29) Yang, Z.; Du, G.; Guo, Z.; Yu, X.; Chen, Z.; Guo, T.; Liub, H. *J. Mater. Chem.* **2011**, *21*, 8591−8596.

(30) Yang, Z.; Du, G.; Guo, Z.; Yu, X.; Chen, Z.; Guo, T.; Zeng, R. *Nanoscale* **2011**, *3*, 4440−4447.

(31) Liu, S.; Jia, H.; Han, L.; Wang, J.; Gao, P.; Xu, D.; Yang, J.; Che, S. *Adv. Mater.* **2012**, *24*, 3201−3204.

(32) Kobayashi, M.; Petrykin, V.; Kakihana, M. *Chem. Mater.* **2007**, *19*, 5373−5376.

(33) Xiang, G.; Wang, Y. G.; Li, J.; Zhuang, J.; Wang, X. *Sci. Rep.* **2013**, *3*, 1411.

(34) Joo, J.; Kwon, S. G.; Yu, T.; Cho, M.; Lee, J.; Yoon, J.; Hyeon, T. *J. Phys. Chem. B* **2005**, *109*, 15297−15302.

(35) LLB Powder Diffraction Software Site Home Page. http://www-llb.cea.fr/fullweb.

(36) Buonsanti, R.; Carlino, E.; Giannini, C.; Altamura, D.; De Marco, L.; Giannuzzi, R.; Manca, M.; Gigli, G.; Cozzoli, P. D. *J. Am. Chem. Soc.* **2011**, *133*, 19216−19239.

(37) De Marco, L.; Manca, M.; Buonsanti, R.; Giannuzzi, R.; Malara, F.; Pareo, P.; Martiradonna, L.; Giancaspro, N. M.; Cozzoli, P. D.; Gigli, G. *J. Mater. Chem.* **2011**, *21*, 13371−13379.

(38) Liu, Y.; Clark, M.; Zhang, Q.; Yu, D.; Liu, D.; Liu, J.; Cao, G. *Adv. Energy Mater.* **2011**, *1*, 194−202.

(39) Lin, Y. H.; Wei, T. Y.; Chien, H. C.; Lu, S. Y. *Adv. Energy Mater.* **2011**, *1*, 901−907.

(40) Belviso, M. R.; Carlino, E., Giannini, C., Scremin, B. F., Cozzoli, P. D. manuscript in preparation

(41) Pietsch, U.; von Hol, V.; Baumbach, T. *High-Resolution X-ray Scattering from Thin Films to Lateral Nanostructures*, 2nd ed.; Springer: New York, 2004.

(42) Lindstrom, H.; Sodergren, S.; Solbrand, A.; Rensmo, H.; Hjelm, J.; Hagfeldt, A.; Lindquist, S. *J. Phys. Chem. B* **1997**, *101*, 7717−7722.

(43) Wagemaker, M.; Kentgens, A. P. M.; Mulder, F. M. *Nature* **2002**, *418*, 397−399.

(44) Lunell, S.; Stashans, A.; Ojamäe, L.; Lindström, H.; Hagfeldt, A. *J. Am. Chem. Soc.* **1997**, *119*, 7374−7380.

(45) Wang, H.; He, J.; Boschloo, G.; Lindström, H.; Hagfeldt, A.; Lindquist, S. E. *J. Phys. Chem. B* **2001**, *105*, 2529−2533.

(46) Boschloo, G.; Fitzmaurice, D. *J. Phys. Chem. B* **1999**, *103*, 2228−2231.

(47) Kavan, L.; Kratochvilova, K.; Graetzel, M. *J. Electroanal. Chem.* **1995**, *394*, 93−102.

(48) Kavan, L.; Gratzel, M.; Rathousky, J.; Zukal, A. *J. Electrochem. Soc.* **1996**, *143*, 394−400.

(49) Beuvier, T.; Richard-Plouet, M.; Brohan, L. *J. Phys. Chem. C* **2009**, *113*, 13703−13706.

(50) Fröschl, T.; Hörmann, U.; Kubiak, P.; Kučerová, G.; Pfanzelt, M.; Weiss, C. K.; Behm, R. J.; Hüsing, N.; Kaiser, U.; Landfester, K.; Wohlfahrt-Mehrens, M. *Chem. Soc. Rev.* **2012**, *41*, 5313−5360.

(51) Nam, S. H.; Shim, H. S.; Kim, Y. S.; Dar, M. A.; Kim, J. G.; Kim, W. B. *ACS Appl. Mater. Interfaces* **2010**, *2*, 2046−2052.

(52) Kim, H.; Kim, M. G.; Shin, T. J.; Shin, H. J.; Cho. J. *Electrochem. Commun.* **2008**, *10*, 1669−1672.

(53) Guo, Y. G.; Hu, Y. S.; Sigle, W.; Maier, J. *Adv. Mater.* **2007**, *19*, 2087−2091.

(54) Qiu, Y. C.; Yan, K. Y.; Yang, S. H.; Jin, L. M.; Deng, H.; Li, W. S. *ACS Nano* **2010**, *4*, 6515−6526.

(55) Das, S. K.; Patel, M.; Bhattacharyya, A. J. *ACS Appl. Mater. Interfaces* **2010**, *2*, 2091−2099.

(56) Das, S. K.; Darmakolla, S.; Bhattacharyya, A.J. *J. Mater. Chem.* **2010**, *20*, 1600−1606.

(57) Cao, F. F.; Wu, X. L.; Xin, S.; Guo, Y. G.; Wan, L. J. *J. Phys.Chem. C* **2010**, *114*, 10308−10313.

(58) Bard, A. J.; Faulkner, L. R. *Electrochemical Methods: Fundamentals and Applications*; John Wiley and Sons: New York, 1980.

(59) Armstrong, R. A.; Armstrong, G.; Canales, J.; Bruce, P. G. *J. Power Sources* **2005**, *146*, 501−506.

(60) Zhou, Y.; Cao, L.; Zhang, F.; He, B.; Li, H. *J. Electrochem. Soc.* **2003**, *150*, A1246−A1249.

(61) Krtil, P.; Fattakhova, D. *J. Electrochem. Soc.* **2001**, *148*, A1045−A1050.

(62) Wang, J.; Zhou, Y.; Hu, Y.; O'Hayre, R.; Shao, Z. *J. Phys. Chem. C* **2011**, *115*, 2529−2536.

(63) Barsoukov, E.; Macdonald, J. R. *Impedance Spectroscopy: Theory, Experiment, and Applications*; John Wiley & Sons: Hoboken, NJ, 1987.

(64) Funabiki, A.; Inaba, M.; Ogumi, Z.; Yuasa, S.; Otsuji, J.; Tasaka, A. *J. Electrochem. Soc.* **1998**, *145*, 172−178.

(65) Levi, M. D.; Lu, Z.; Aurbach, D. *Solid State Ionics* **2001**, *143*, 309−318.

(66) Ho, C.; Raistrick, I. D.; Huggins, R. A. *J. Electrochem. Soc.* **1980**, *127*, 343−350.

(67) Stashans, A.; Lunell, S.; Bergstrom, R.; Hagfeldt, A.; Lindquist, S. E. *J. Phys. Rev. B* **1996**, *53*, 159−170.

(68) Arrouvel, C.; Parker, S. C.; Islam, M. S. *Chem. Mater.* **2009**, *21*, 4778−4783.

(69) Panduwinata, D.; Gale, J. D. *J. Mater. Chem.* **2009**, *19*, 3931−3940.

(70) Lee, S.H.; Cheong, H. M.; Tracy, C. E.; Mascarenhas, A.; Czanderna, A. W.; Deb, S. K. *Appl. Phys. Lett.* **1999**, *75*, 1541−1543.

(71) Wang, J. M.; Khoo, E.; Lee, P. S.; Ma, J. *J. Phys. Chem. C* **2008**, *112*, 14306−14312.

(72) Subrahmanyam, A.; Karuppasamy, A. *Sol. Energy Mater. Sol. Cells* **2007**, *91*, 266−274.

(73) Chen, J. Z.; Ko, W. Y.; Yen, Y. C.; Chen, P. H.; Lin, K. J. *ACS Nano* **2012**, *6*, 6633−6639.